Iodine chemistry determines the defect tolerance of lead-halide perovskites

Daniele Meggiolaro,[a,b] Silvia G. Motti,[c,d] Edoardo Mosconi,[a,b] , Alex Barker[c], James Ball,[c] Carlo Andrea Riccardo Perini,[c] Felix Deschler,[e] Annamaria Petrozza,[c] Filippo De Angelis[a,b]

[a] Computational Laboratory for Hybrid/Organic Photovoltaics (CLHYO), CNR-ISTM, Via Elce di Sotto 8, 06123, Perugia, Italy.

[b] CompuNet, Istituto Italiano di Tecnologia, Via Morego 30, 16163 Genova, Italy.

[c] Center for Nano Science and Technology @Polimi, Istituto Italiano di Tecnologia, via Giovanni Pascoli 70/3, 20133, Milan, Italy.

[d] Dipartimento di Fisica, Politecnico di Milano, Piazza Leonardo da Vinci, 32, 20133 Milano, Italy.

[e]Cavendish Laboratory, University of Cambridge, JJ Thomson Avenue, Cambridge, CB3 0HE, UK

Supplementary Information

1.1 SHR theory:

Trapping at defects induces non-radiative recombination, whose rate (R) is defined as:

$$R = \frac{np - n_i^2}{\tau_p(n + n_1) + \tau_n(p + p_1)} \qquad (1)$$

where n, p, and n_i are the electron/hole carrier densities and intrinsic carriers density, respectively; $\tau_{p,n}$ are the holes and electrons lifetimes; $n_1 = N_C exp(-\frac{E_c - E_T}{kT})$ and $p_1 = N_V exp(-\frac{E_T - E_V}{kT})$; and E_T is the energy of the considered trap (E_C and E_V are the conduction and valence band energies, with related N_C and N_V density of states).

1.2 Accuracy of calculated DFEs

The DFEs have been calculated by using the equation

$$DFE(X^q) = E(X^q) - E(perf) - \sum_i n_i\mu_i + q(E_F + V + \Delta V) + E^q(corr) \quad (2)$$

where $E(X^q)$ is the energy of the defect supercell, $E(perf)$ the energy of the pristine supercell, n and μ are the number and the chemical potentials of the species added or subtracted to the perfect bulk in order to form the defect. The last term represents the energy associated to the exchange of electrons with the electrons reservoir (the Fermi level of the system), referenced to the valence band maximum (VBM) of the pristine crystal and corrected for the electrostatic potential shift and the charged defects images interactions. The chemical potentials of the atomic species have been set in order to simulate three different chemical conditions, namely I-rich, I-medium and I-poor conditions, under the constraint of the thermodynamic stability of the $MAPbI_3$ phase. The chemical potentials of $MAPbI_3$ constituents, i.e. Pb, I and MA, in thermodynamic equilibriums with the PbI_2 and MAI phases, have been evaluated by imposing the following relations among the chemical potentials

$$\mu(MA) + \mu(Pb) + 3\mu(I) = \Delta_f H(MAPbI_3) \quad (3)$$

$$\mu(MA) + \mu(I) < \Delta_f H(MAI) \quad (4)$$

$$\mu(Pb) + 2\mu(I) = \Delta_f H(PbI_2) \quad (5)$$

where the chemical potentials of the species I and Pb has been referenced to the value of the I_2 molecule and Pb bulk metal, respectively.

A preliminary analysis carried out at different levels of theory confirms that for an accurate estimate of the DFEs in $MAPbI_3$ inclusion of both spin-orbit coupling and exact exchange are essential. These affect two main terms of the DFEs energies (Equation 2 above), namely the lattice energy due to the relaxation of the ions upon the formation of the defect and the electronic energy due to the charge exchange with the Fermi level. While the Perdew-Burke-Ernzerhof (PBE)[1] exchange-correlation functional provides good geometries and lattice energies, the electronic

structure of the perovskite obtained by this approximation is not sufficiently accurate for a correct estimate of the DFEs.

The equilibrium geometries of the defects supercells and simple phases, i.e. PbI_2, MAI and I_2, have been found by using the PBE exchange-correlation functional. US pseudopotentials with a cutoff on the plane waves of 40 Ryd (320 Ryd on the charge density) and converged uniform k-points grids in the Brillouin zone (BZ) have been used. For defective supercells, with lattice constants of a=b=17.698 Å, c=12.642 Å, calculations have been performed by using the 1x1x2 kpoint grids in the Brillouin Zone (BZ). Pseudopotentials with 7, 4, 5 and 1 valence electrons have been used for I, C, N and H, while a 14 valence electrons pseudopotential for the Pb element has been used by including semi-core Pb 5d states. The band edges of $MAPbI_3$ are characterized by large contributions of the I 5p orbitals to the top of the valence band (VB), with minor contributions of the Pb s states, while the bottom of the conduction band is dominated by the Pb 6p orbitals. The inclusion of spin orbit coupling (SOC) with the same converged parameters of above leads to a remarkable decrease of the band gap to a value of 0.55 eV. As expected, the inclusion of SOC at the PBE level leads to a large stabilization of the unoccupied 6p state of Pb of about 0.8 eV and to a destabilization of the occupied 5p states of I ions of about 0.19 eV. [2]

Heats of formation of the $MAPbI_3$ phase starting from the PbI_2 and MAI have been obtained of -0.15 and -0.18 eV at the PBE and PBE-SOC levels of theory, highlighting a limited stability of the $MAPbI_3$ perovskite. The self-interaction error responsible of the strong underestimate of the band gap has been corrected by introducing a fraction of exact exchange through the HSE06 functional [3] (α=0.43), following the approach of Du.[4] Hybrid calculations, spin orbit coupling included, have been carried out at the relaxed PBE geometries and by using norm-conserving (NC) pseudopotentials. A norm conserving pseudopotential with 22 valence electrons for Pb has been used, by including the Pb 5s and 5p states, which ensures an accurate reproduction of $MAPbI_3$ band gap and band edges against GW calculations.[5] For the other elements, pseudopotentials with the same number of valence electrons as in the US case have been used. To reduce the computational

effort, hybrid SOC calculations have been performed by using a plane wave cutoff of 40 Ryd, without affecting the accuracy of the calculations. In table S1 and S2 a comparison of calculated DFEs at the PBE-SOC level with 14 electrons Pb US pseudopotentials (cutoff on the plane waves of 40 Ryd, 320 Ryd on the charge density) and NC pseudopotentials with the 22 electrons Pb pseudopotential (cutoff on the plane waves 40 Ryd) is reported. Two hybrid benchmark calculations have been also performed for I_i and V_{Pb}^{2-} defects by using a cutoff on plane waves of 70 Ryd. The calculated DFEs for these two defects in I-rich conditions are 0.88 and 0.84 eV for I_i and V_{Pb}^{2-} respectively, to be compared with results obtained with a cutoff of 40 Ryd of 0.93 and 0.83 eV. As it can be seen, only limited deviations in the results are reported, confirming the good convergence of our calculations.

By using the HSE06 functional and including the SOC a band gap of 1.58 eV has been obtained for $MAPbI_3$, in good agreement with experiments and previous calculations.[2,4] The calculated electronic band edges at the HSE06-SOC level reports a large downshift of the VB and CB of 0.53 eV and 0.5 eV compared to the PBE level of theory, see Figure S2. The shift of the band edges obtained by using the HSE06 functional are also in agreement with results of a benchmark G_0W_0 calculation,[5] confirming the reliability of our approach.

The DFEs calculated by the PBE, PBE-SOC and HSE06-SOC levels of theory are reported in Figure S1, for I-rich, I-medium and I-poor conditions, without including dispersion corrections for a direct comparison of electronic energies. Furthermore, the values of the calculated DFEs at E_F=0 (VBM) for neutral and charged defects have been reported in Table S1 and S2. As it can be seen the calculated DFEs show strong deviations among the different levels of theory. The inclusion of SOC at the PBE level leads to the overall stabilization of neutral defects (see Table S1), while regarding charged defects a stabilization of negative charged species and a destabilization of positive species, proportionally to the charge of the defect, is seen (Table S2). The opposite occurs at the HSE06-SOC level.

The inclusion of SOC and exact exchange in the HSE06-SOC calculations clearly points out the emergence of new deep levels in the band gap compared to the PBE approach, as in the case of the (0/-) and (-/2-) transitions of I_i and I_{MA} defects (Figure S2). These results are in good agreement with previous results by Du.[4] Furthermore, higher native Fermi levels calculated at the HSE06-SOC levels, compared to PBE calculations are found (Figure S1).

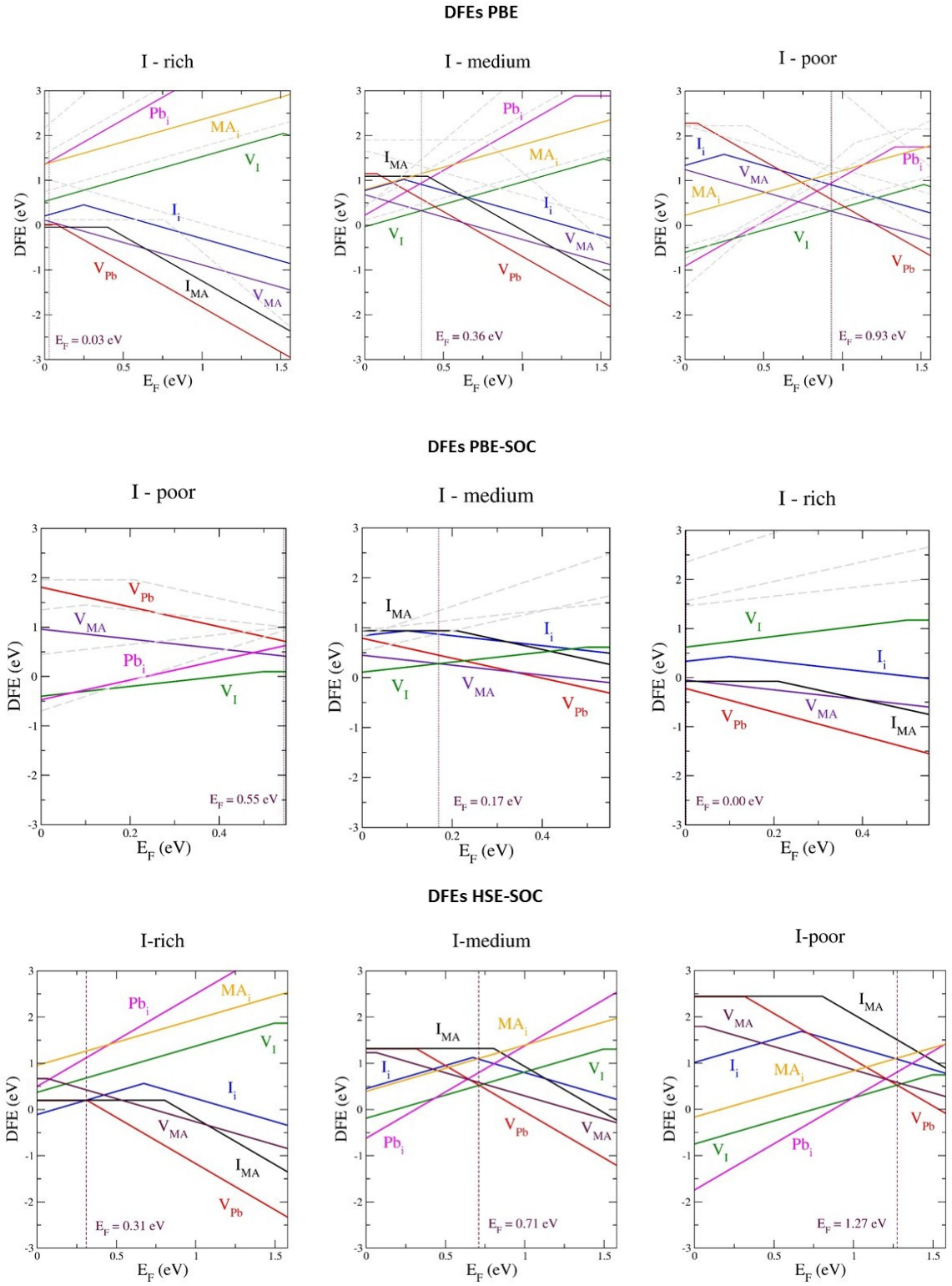

Figure S1. DFE diagrams calculated at the PBE, PBE-SOC and HSE06 levels of theory for I-rich, I-medium and I-poor conditions of growth (dispersions corrections not included).

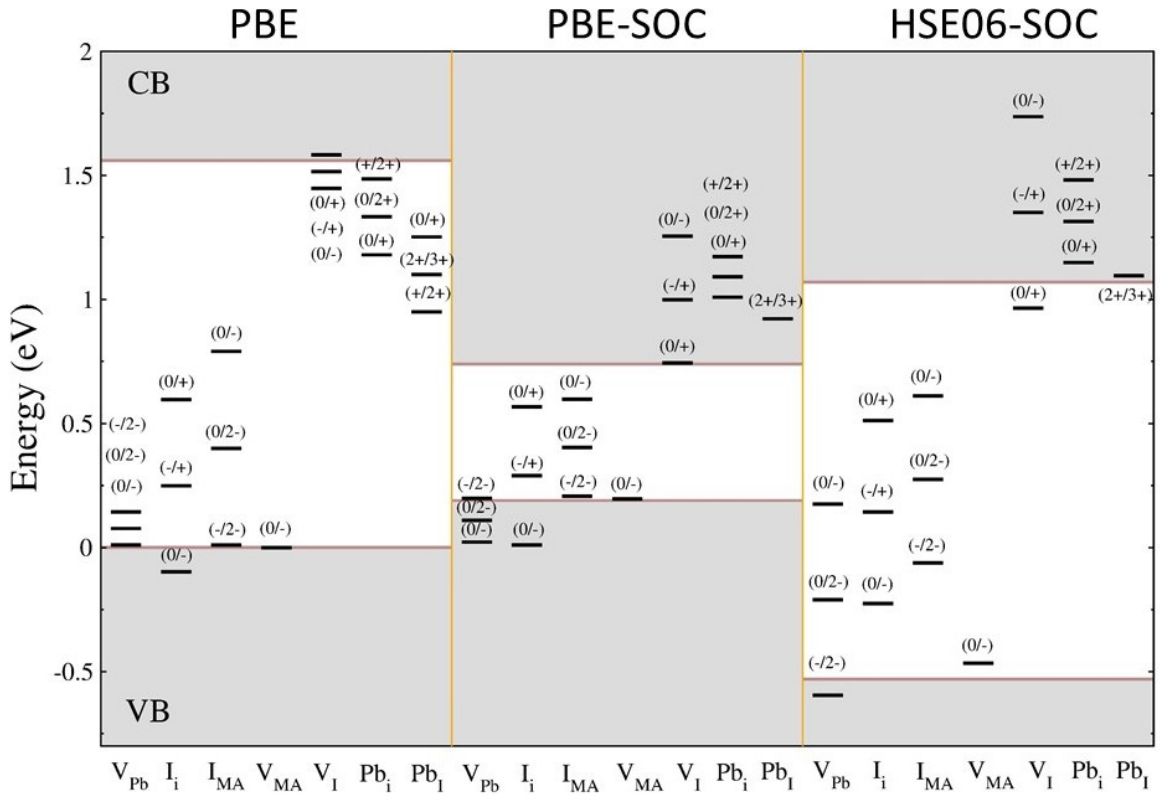

Figure S2. Thermodynamic ionization diagrams calculated at the PBE, PBE-SOC and HSE06-SOC levels of theory (no dispersion included).

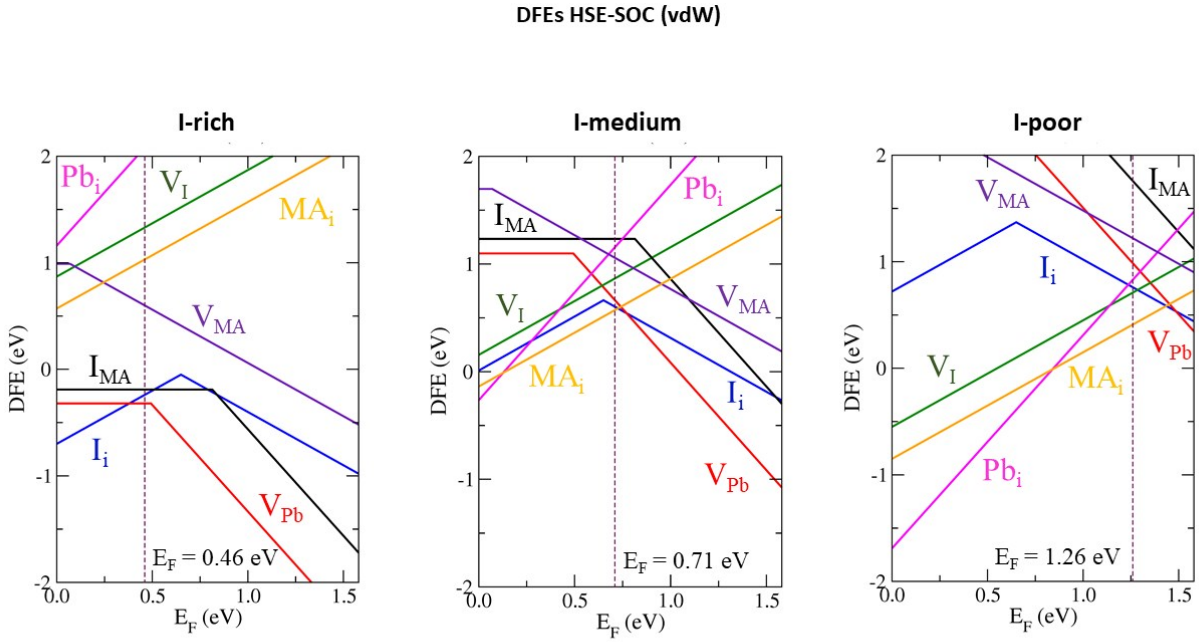

Figure S3. DFEs diagrams calculated at the HSE06-SOC (0.43) level in I-rich, I-medium and I-poor conditions after adding dispersion corrections through the DFT-D3 method.

Table S1. Influence of the spin-orbit coupling and the electronic exchange on the DFEs of neutral defects in I-rich conditions. US calculations have been carried out by using US pseudopotentials (Pb 14 electrons) and a cutoff on PWs of 40 Ryd (320 Ryd for the charge density). NC* calculations have been carried out by using the 22 electrons Pb pseudo and a cutoff of 40 Ryd on the PWs.

(eV)	$\mathbf{V_I}$	$\mathbf{I_i}$	$\mathbf{V_{Pb}}$	$\mathbf{Pb_i}$	$\mathbf{I_{MA}}$	$\mathbf{V_{MA}}$
PBE (US)	2.11	0.80	0.01	4.02	-0.04	0.11
PBE-SOC (US)	1.17	0.71	-0.06	3.36	-0.08	-0.06
PBE-SOC (NC*)	1.19	0.77	-0.04	3.39	-0.10	-0.08
HSE06-SOC (NC*)	1.87	0.93	0.19	4.19	0.20	0.67

Table S2. Influence of the spin-orbit coupling and the electronic exchange on the DFEs of charged defects calculated at E_F=0 in I-rich conditions. Values are in eV. US calculations have been carried out by using US pseudopotentials (Pb 14 electrons) and a cutoff on PWs of 40 Ryd (320 Ryd for the charge density). NC* calculations have been carried out by using the 22 electrons Pb pseudo and a cutoff of 40 Ryd on the PWs.

Acceptors	$\mathbf{V_{Pb}^{2-}}$	$\mathbf{I_i^-}$	$\mathbf{V_{MA}^-}$	$\mathbf{I_{MA}^{2-}}$
PBE (US)	0.21	0.70	0.11	0.83

PBE-SOC (US)	-0.18	0.53	-0.06	0.43
PBE-SOC (NC*)	-0.33	0.57	-0.06	0.46
HSE06-SOC (NC*)	0.87	1.24	0.73	1.8
Donors	**V_I^+**	**Pb_i^{2+}**	**MA_i^+**	**Pb_I^{3+}**
PBE (US)	0.53	1.33	1.36	2.05
PBE-SOC (US)	0.62	1.54	1.46	2.35
PBE-SOC (NC*)	0.60	1.41	1.51	2.22
HSE06-SOC (NC*)	0.37	0.48	0.95	0.89

Table S3. Stable states of charge, DFEs and defect densities calculated at the native Fermi level in iodine-medium conditions.

Defect	Charge	DFE (eV)	Density (cm^{-3})
$\mathbf{V_{Pb}}$	2-	0.66	~ 10^{10}
$\mathbf{MA_i}$	+	0.57	~ 10^{12}
$\mathbf{I_i}$	+ / -	0.72/0.60	~ $10^{10}/10^{12}$
$\mathbf{V_I^+}$	+	0.87	~ 10^{7}
$\mathbf{Pb_i^{2+}}$	2+	1.16	~ 10^{2}
$\mathbf{V_{MA}}$	-	1.06	~ 10^{4}
$\mathbf{I_{MA}}$	2-	1.44	~ 0

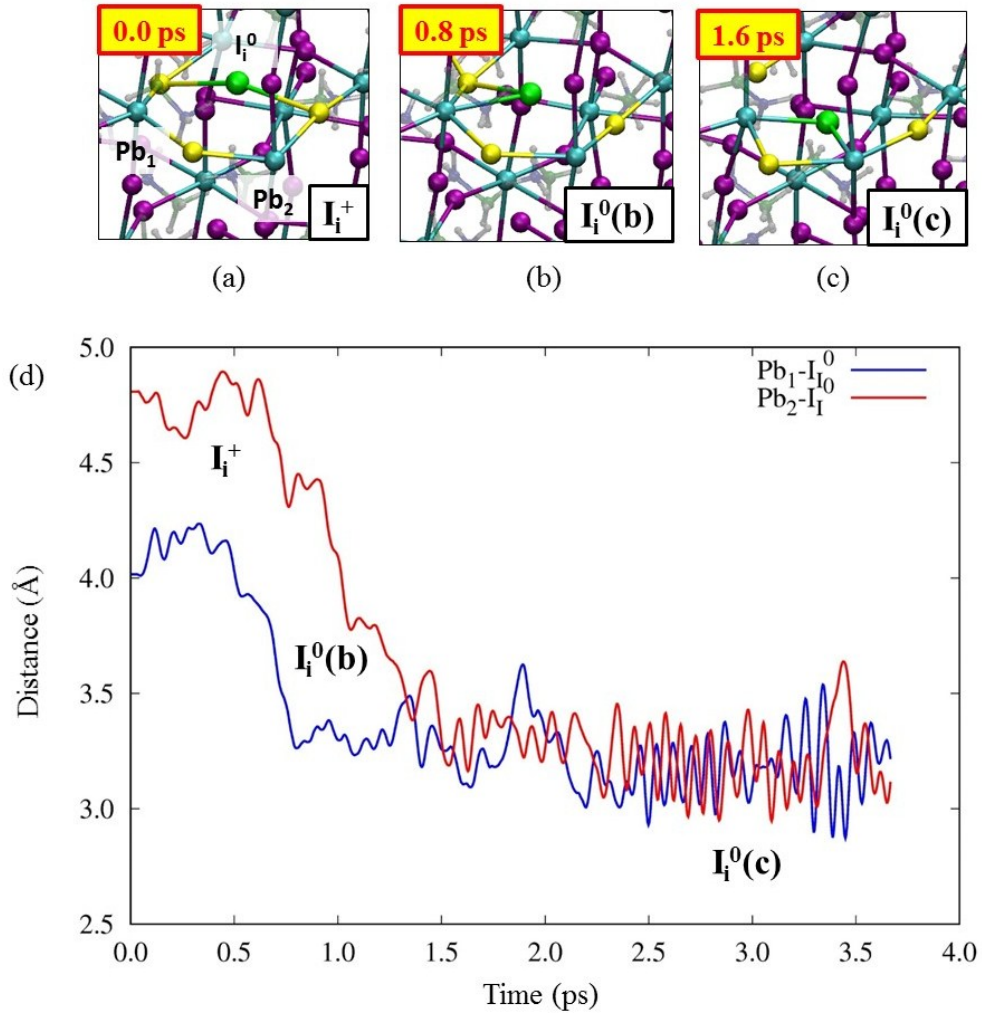

Figure S4. The search for the stable configurations of the I_i interstitial performed at the PBE level highlighted the existence of several minima in the configuration space. In order to investigate this aspect, a molecular dynamics simulations of the neutral interstitial defect have been performed, aimed to provide an accurate description of the associated configuration space at the PBE level. The MD simulation has been carried out for 4 ps at room temperature starting from the I trimer, the most stable configuration of the positive interstitial I_i^+, and investigating the evolution of the Pb-I distances vs time. After 0.8 ps the interstitial moves toward the I_i^0(b) configuration with two iodines at distance 3.44 Å. After 1.6 ps the distance between iodines further increases to a value of 3.88 Å

in a rhombus in the ab plane, here called I_i^0(c). Both the I_i^0(b) and the I_i^0(c) configurations are less stable than the I_i^0(a) configuration at the HSE06-SOC level of 0.18 and 0.44 eV, respectively.

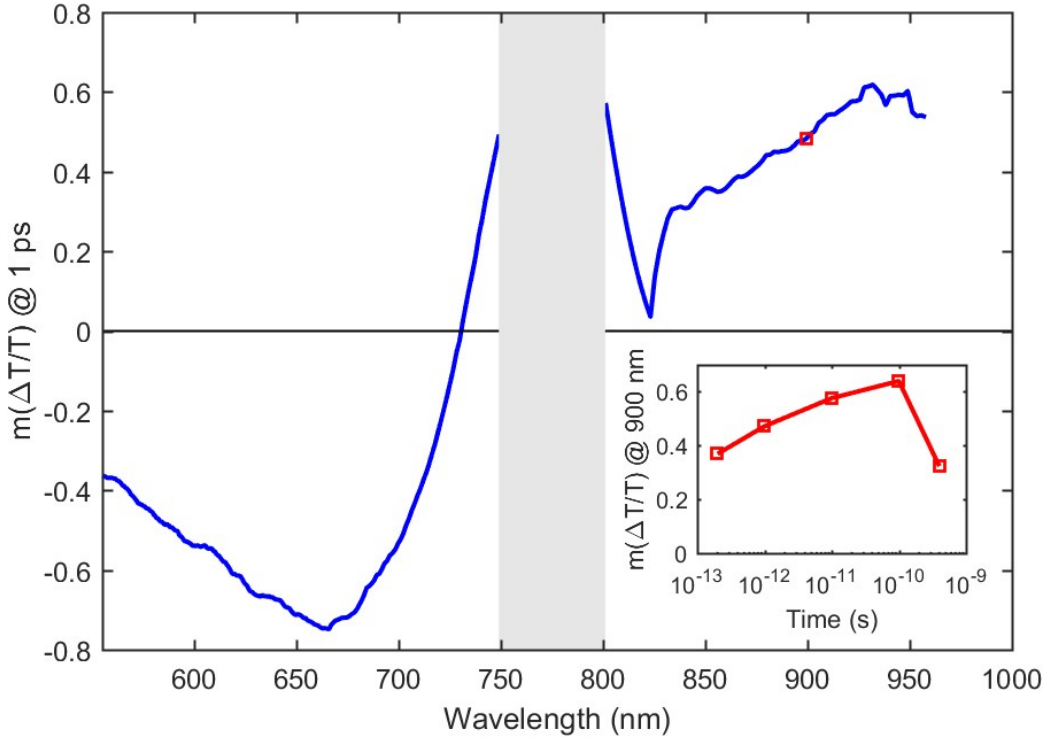

Figure S5. Transient absorption spectrum (at 1 ps pump-probe delay) of a hole-defect rich thin film showing the photo-bleach band (>850 nm) belonging to the sub-bandgap emissive states observed in Figure 3a. Inset: evolution in time of the sub-bandgap feature at 900 nm.

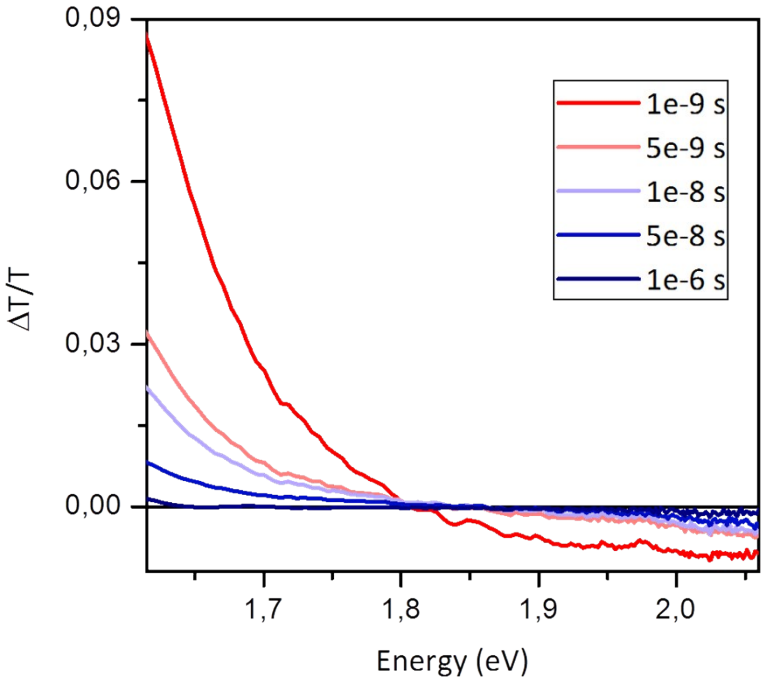

Figure S6. Transient absorption spectra of $MAPbI_3$ at various delay times.

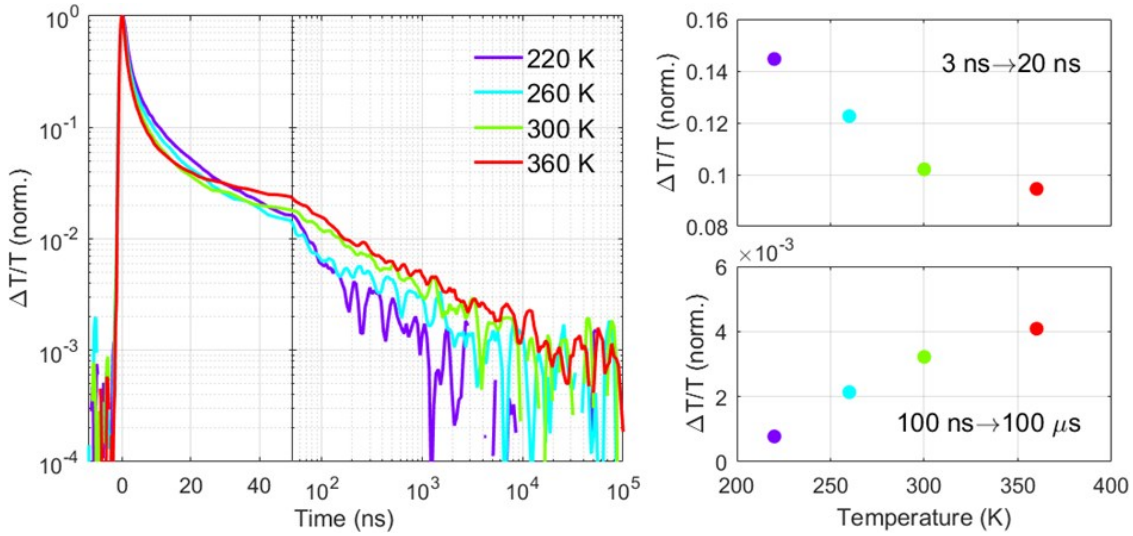

Figure S7. $MAPbI_3$: Temperature dependent transient absorption shows fast recombination due to emissive band-to-band recombination at early times (up to ~30 ns), followed by extremely slow recombination of trapped electrons. With increasing temperature, we see faster band-to-band recombination, and a higher number of long-lived trapped electrons.

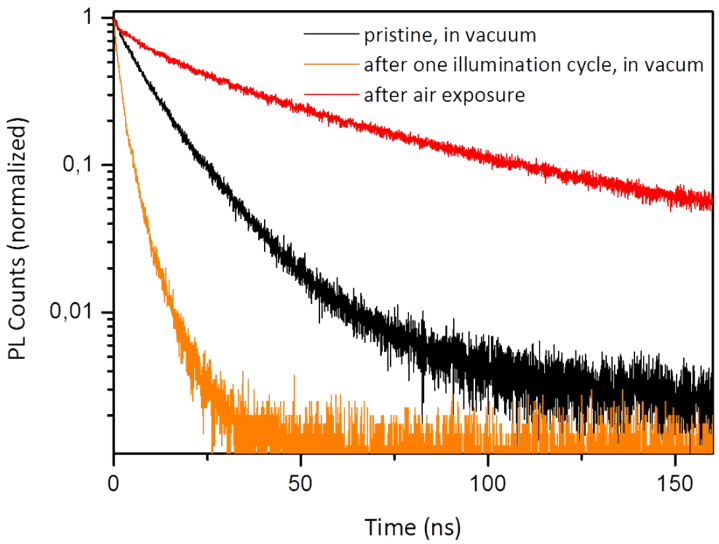

Figure S8. PL decays recorded at 1.58 eV, peak of the PL spectrum of $MAPbI_3$, and assigned to band-to-band carrier recombination. These dynamics are all measured at approximately 5×10^{15} cm^{-3} excitation density. The black line is the decay belonging to the pristine sample, measured in running vacuum, while the orange line is the decay measured in vacuum after exposing the sample to an excitation density cycle going from 5×10^{15} cm^{-3} to 10^{18} cm^{-3} and then back to 5×10^{15} cm^{-3}. This highlights the formation of defect states upon photo-excitation. Eventually, these defect states are passivated by oxygen upon O_2 exposure (see Motti et al).[6]

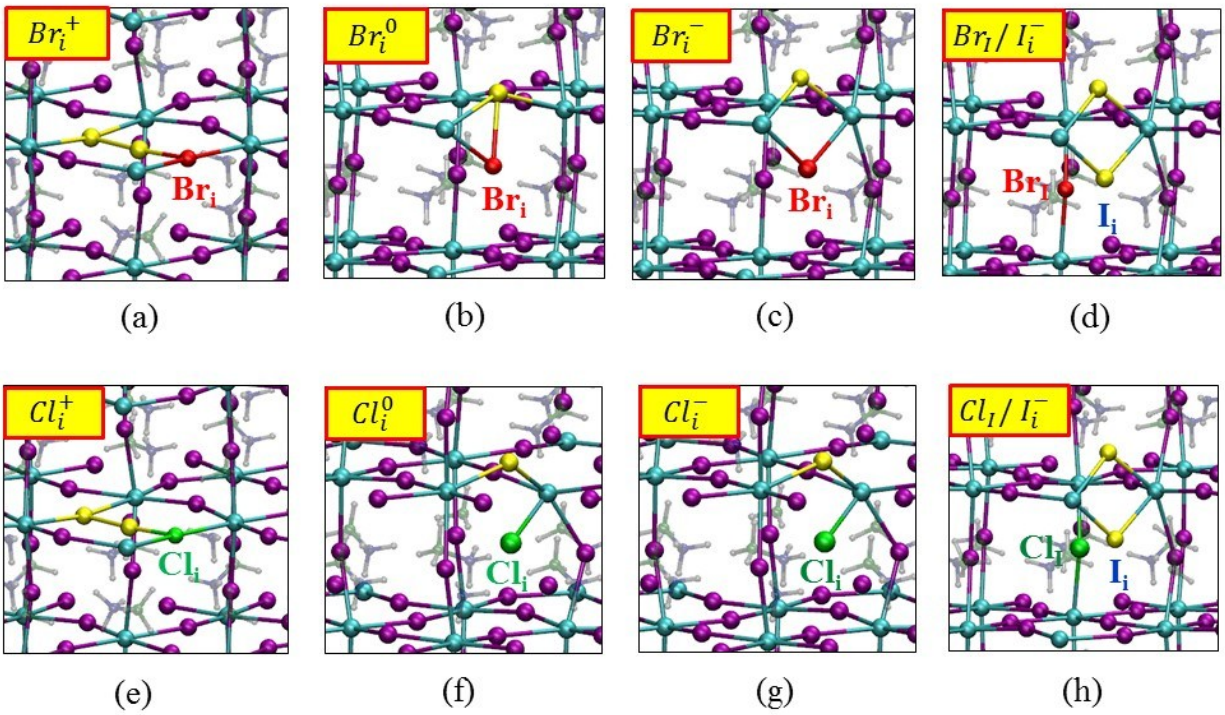

Figure S9. a-d) Equilibrium structures of the positive, neutral, negative Br interstitials and of the negative I interstitial with a substitutional Br_I, respectively. e-h) Equilibrium structures of the positive, neutral, negative Cl interstitials, and of the negative I interstitial with a substitutional Cl_I, respectively.

Table S4. Defects formation energies of substitutional and interstitials iodine, bromine and chlorine in the lowest doping limits at the native Fermi level of the $MAPbI_3$ in I-medium conditions. The DFEs have been calculated for the different states of charge at the HSE-SOC (0.43) level of theory, by including dispersions. A direct comparison of the energies calculated for a supercell with iodine interstitial and a substitutional Br (Cl) on the I site and a supercell with Br (Cl) interstitials, both in the negative states, shows that the substitution of I interstitial by a Br (Cl) ion is favoured by 0.07 eV (0.07 eV), as calculated at the HSE-SOC (0.43) level.

DFEs (eV)	**(+)**	**0**	**(-)**
I_i	0.66	1.02	0.66
Br_i	0.74	1.12	0.50
Br_I	0.02	0.02	0.02
Cl_i	0.81	1.02	0.37
Cl_I	0.01	0.01	0.01

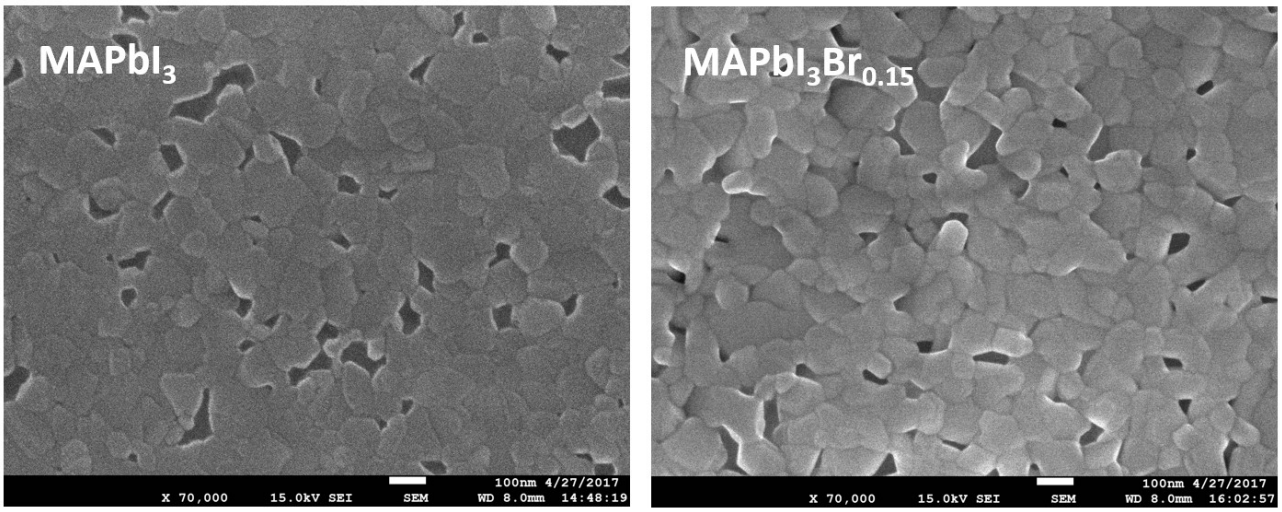

Figure S10. SEM micrographs of $MAPbI_3$ and $MAPbI_3Br_{0.15}$

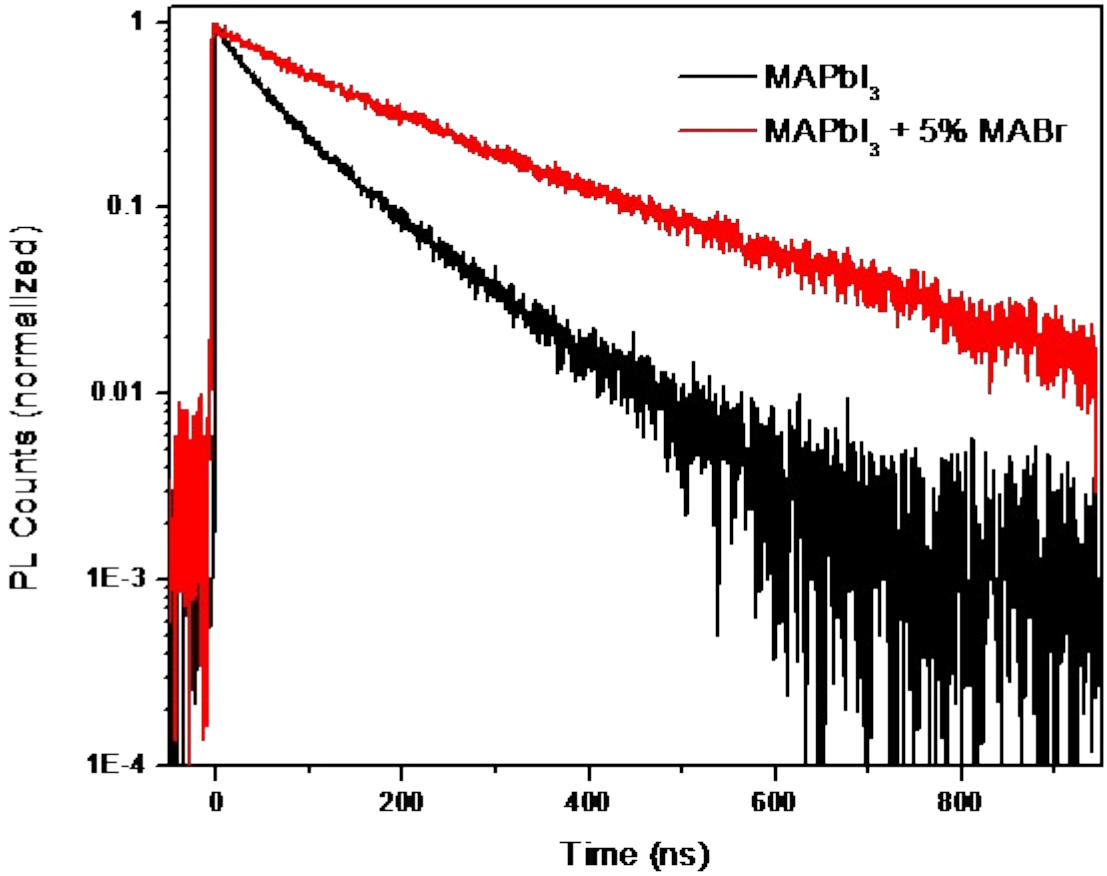

Figure S11. PL decays recorded at 1.58 eV, peak of the PL spectrum of $MAPbI_3$, assigned to band-to-band carrier recombination. The black line corresponds to the control $MAPbI_3$ sample, while the red line is the decay of the sample prepared with addition of 5% MABr in the precursor solution.

Both dynamics were measured at approximately 2×10^{14} cm^{-3} excitation density and under active vacuum.

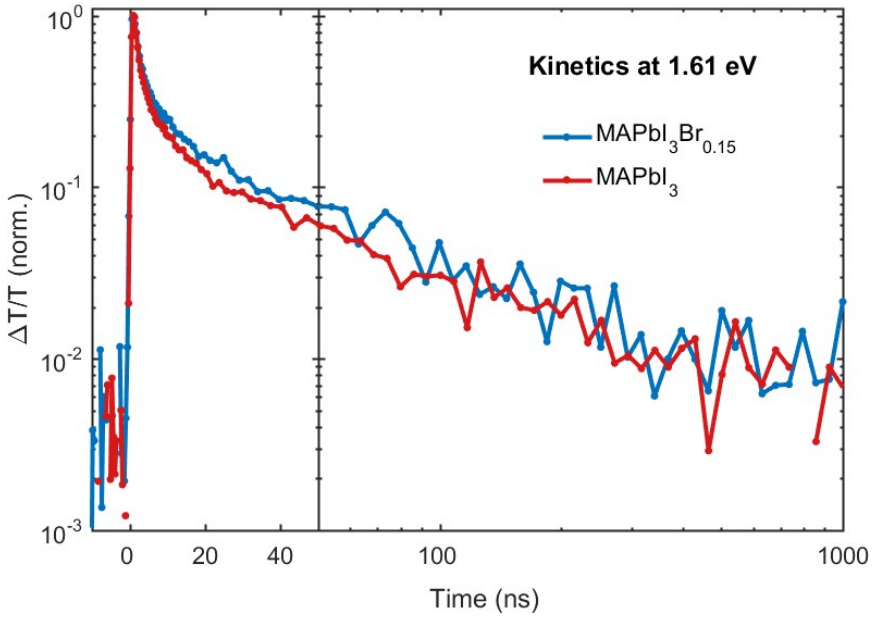

Figure S12. TA dynamics probed at the photo-bleach band at 1.61 eV of the transient absorption spectrum of $MAPbI_3$ (red line) and $MAPbI_3Br_{0.15}$ (blue line).

Table S5. Influence of the fraction of exact exchange (EXX) α on a selected list of thermodynamic and electronic properties of the $MAPbI_3$, PbI_2 and I_2 phases and on the defect formation energy of the iodine interstitials as calculated by the HSE06 functional and including spin orbit corrections.

System	Quantity	EXX α=0.25	EXX α=0.43
$MAPbI_3$	Heat of formation (kJ/mol)	-0.10	-0.06
	Band gap (eV) [exp. 1.60]	1.09	1.58
PbI_2	Heat of formation (kJ/mol)	-209.8	-215.4
	Band gap (eV) [exp. ~2.49]	1.87	2.44
I_2	Binding energy (eV) [exp. 1.57]	1.58	1.49
I_i^-	DFE (E_F=0, I-rich, eV)	0.94	1.24
I_i	DFE (E_F=0, I-rich, eV)	0.87	0.93
	(0/-) transition (eV)	0.07	0.30

Table S6. Calculated DFEs at the PBE level of the main neutral defects in the bulk and on the PbI2 terminated surface of the $MAPbI_3$ perovskite in I-medium conditions

Defect	DFE Bulk (eV)	DFE Surface (eV)
I_i	1.37	0.07
V_I	1.55	1.00
Pb_i	2.89	1.99
V_{Pb}	1.15	0.64

References

1. Perdew, J. P.; Burke, K.; Ernzerhof, M., Generalized Gradient Approximation Made Simple. Phys. Rev. Lett. **1996**, 77, 3865-3868.
2. Mosconi, E.; Amat, A.; Nazeeruddin, M. K.; Graetzel, M.; De Angelis, F., First-Principles Modeling of Mixed Halide Organometal Perovskites for Photovoltaic Applications. Journal of Physical Chemistry C **2013**, 117, 13902−13913.
3. Heyd, J.; Scuseria, G. E.; Ernzerhof, M., Hybrid functionals based on a screened Coulomb potential. The Journal of Chemical Physics **2003**, 118, 8207-8215.
4. Du, M.-H., Density Functional Calculations of Native Defects in CH3NH3PbI3: Effects of Spin–Orbit Coupling and Self-Interaction Error. J. Phys. Chem. Lett. **2015**, 6, 1461-1466.
5. Umari, P.; Mosconi, E.; De Angelis, F., Relativistic GW calculations on $CH_3NH_3PbI_3$ and $CH_3NH_3SnI_3$ Perovskites for Solar Cell Applications. Sci. Rep. **2014**, 4, 4467.
6. Motti, S. G.; Gandini, M.; Barker, A. J.; Ball, J. M.; Srimath Kandada, A. R.; Petrozza, A., Photoinduced Emissive Trap States in Lead Halide Perovskite Semiconductors. ACS Energy Letters **2016**, 1, 726-730.